Progress In Electromagnetics Research C, Vol. 123, 75–89, 2022

A Fault-Tolerant Control Strategy for D-PMSG Wind Power Generation System

Bing Luo[1, 2], Sicheng Peng[1], Yang Zhang[1, *], Zihao Liu[1], and Bo Huang[1]

Abstract—Aiming at the problem of motor speed decrease in direct-drive permanent magnet synchronous generator (D-PMSG) wind power generation system after permanent magnet (PM) demagnetization faults, a demagnetization fault-tolerant control strategy in D-PMSG wind power generation system is proposed. Firstly, the D-PMSG mathematical model is described in normal and demagnetization. Secondly, an extended Kalman filter (EKF) observer is designed to observe the PM flux online. Then, flux linkage parameters are introduced into the two-vector model predictive fault-tolerant control so that the increase of stator current is controlled within the limit range. Meanwhile, the motor speed can follow the change of the given speed. In addition, the improved Luenberger mechanical torque observer is designed in the speed outer ring to deal with the vibration caused by unstable wind speed. Finally, compared with the dual-closed-loop Proportional Integral (PI) control, the experimental results show that the demagnetization fault-tolerant control strategy has smaller speed overshoot and smaller speed fluctuation when the mechanical torque changes. The method can maintain the speed balance when the PM demagnetization faults occur and have stronger fault tolerance and anti-interference ability.

1. INTRODUCTION

Compared with doubly-fed wind power generation system, the direct-drive permanent magnet synchronous generator (D-PMSG) wind power generation system composed of D-PMSG is connected to the large power grid through back-to-back converters to achieve decoupling control between the machine and the power grid [1, 2]. D-PMSG wind power generation system does not need excitation devices, resulting in higher power generation efficiency and stability. D-PMSG wind power generation system will become the mainstream type of wind power generation [3, 4].

After a long-term operation in relatively harsh operating environments such as desert, gobi, and sea surface, the PM in D-PMSG may have demagnetization faults due to high temperature, chemical corrosion, mechanical vibration, and other factors [5, 6]. When a large-scale generator set connected to the grid has demagnetization faults, the terminal voltage of the generator will decrease, and the generator will absorb a large amount of reactive power from the system [7], which will cause fluctuations in the electrical parameters of the power grid and affect the operation safety of the power system.

To avoid the occurrence of demagnetization faults, some scholars optimized the motor structure [8–12]. However, the cost of changing the motor structure is too high, so online detection [13–15] and fault-tolerant control [16, 17] are more promising research directions. In [7], the scholars proposed a new criterion based on motor power angle and synchronous electromotive force for demagnetization fault. In [18], the scholars proposed a new demagnetization protection method to determine the stability of one pendulum and multiple pendulums by measuring the direct power angle. These two methods

---

Received 23 June 2022, Accepted 8 August 2022, Scheduled 23 August 2022

[*] Corresponding author: Yang Zhang (459387623@qq.com).

[1] Hunan University of Technology, Zhuzhou 412007, China. [2] CSG Electric Power Research Institute Co. Ltd, Guangzhou 510663, China.

enhance the selectivity and rapidity of the demagnetization protection of large generator sets. However, both of these methods carry out demagnetization protection at the level of the power system and do not solve the problem of the fault-tolerant control of D-PMSG itself. In [19], fuzzy processing and BP neural network were combined to detect the degree of demagnetization fault of PMSG, but fault-tolerant control was not carried out. Therefore, there is no systematic study on fault-tolerant control of the D-PMSG wind power generation system.

When the demagnetization fault occurs in D-PMSG, the fault-tolerant of conventional wind power generation system is limited, and the generator will stall. The conventional wind power generator system adopts dual-closed-loop Proportional Integral (PI) control on the generator side [20]. When the PM is partially demagnetized, the d-axis flux linkage decreases, and the dual-closed-loop PI controller will increase the stator current to keep the electromagnetic torque unchanged. However, due to the output capacity limitation and overload protection of the converter, the stator current amplitude cannot exceed the limit value. When the stator current reaches the limit, the electromagnetic torque will decrease, and the motor speed will decrease accordingly [21, 22]. However, the speed of D-PMSG is correlated with the wind speed of the wind farm in real-time. When demagnetization faults occur, the motor speed will be disconnected from the wind speed, and the performance of the motor will be greatly reduced. If the wind speed fluctuates greatly at this time, the motor may stop or even burn out [23, 24].

Aiming at the problem that the motor speed decreases after the demagnetization faults in the D-PMSG wind power generation system, this paper proposes a demagnetization fault-tolerant control strategy to realize the stable operation of the D-PMSG wind power generation system even after the demagnetization faults occur. First, the D-PMSG mathematical model in normal and demagnetization is described. Second, an extended Kalman filter (EKF) observer is designed to observe the PM flux online, and the two-vector model predictive fault-tolerant control is proposed based on the EKF observer. Then, an improved Luenberger mechanical torque observer is designed in the outer speed ring to increase its anti-interference capability. The feasibility and effectiveness of the proposed algorithm are verified by comparative experiments. The feasibility and effectiveness of the proposed algorithm are proved by comparative experiments.

2. ANALYSIS OF DEMAGNETIZATION OF D-PMSG

The electromagnetic torque equation of D-PMSG in the d- and q-axis reference frame can be expressed as:

$$T_e = \frac{3}{2} n_p \left(\psi_f + (L_d - L_q) i_d\right) i_q \tag{1}$$

where T_e is the electromagnetic torque; n_p is the number of pole pairs; ψ_f is the flux linkage of PM; L_d and L_q are the d-axis and q-axis stator inductances; i_d and i_q are the d-axis and q-axis stator currents.

The speed equation of D-PMSG is as follows:

$$T_m - T_e - B\omega_r = J \frac{d\omega_r}{dt} \tag{2}$$

When the PM demagnetization fault occurs, the PM flux linkage amplitude and direction will change. The flux linkage amplitude varies from initial ψ_{ro} to ψ_r, and a deviation angle exists between the direction of the rotor flux and the d-axis of the reference frame. It is illustrated in Figure 1.

According to Figure 1, the flux linkage equation of PM of D-PMSG under demagnetization fault is expressed as follows:

$$\begin{cases} \psi_{rd} = \cos\gamma \cdot \psi_r \\ \psi_{rq} = \sin\gamma \cdot \psi_r \end{cases} \tag{3}$$

where ψ_{rd} and ψ_{rq} are the d-axis and q-axis flux linkages of PM.

The stator flux linkage equation of D-PMSG under demagnetization fault is expressed as follows:

$$\begin{cases} \psi_d = \psi_{rd} + L_d i_d \\ \psi_q = \psi_{rq} + L_q i_q \end{cases} \tag{4}$$

where ψ_d and ψ_q are the d-axis and q-axis stator flux linkages.

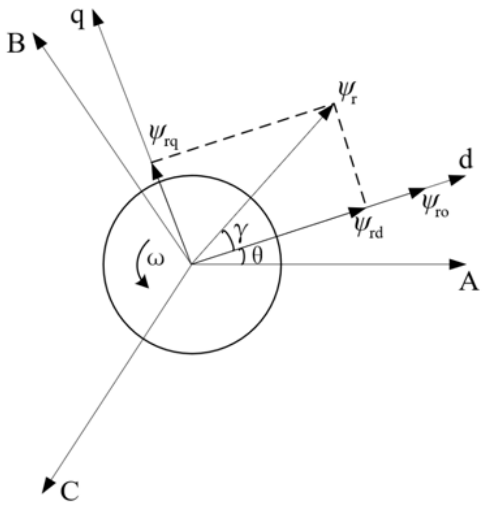

Figure 1. Variation of D-PMSG flux linkage.

Consider that the time constant of the flux changes is much larger than that of the electrical system in the D-PMSG, that is $d\psi_r/dt \approx 0$. Then, state equations of D-PMSG in the d-axis and q-axis reference frames can be expressed as follows when PM demagnetization fault occurs:

$$\begin{cases} \dfrac{di_d}{dt} = -\dfrac{R_s}{L_d} i_d + \omega_e \frac{L_q}{L_d} i_q + \dfrac{u_d}{L_d} + \omega_e \dfrac{\psi_{rq}}{L_d} \\ \dfrac{di_q}{dt} = -\dfrac{R_s}{L_q} i_q - \omega_e \dfrac{L_d}{L_q} i_d + \dfrac{u_q}{L_q} - \omega_e \dfrac{\psi_{rd}}{L_q} \end{cases} \tag{5}$$

For surface D-PMSG, $L_d = L_q = L_s$. The state equation (5) of D-PMSG can be rearranged as follows:

$$\begin{cases} \dfrac{di_d}{dt} = -\dfrac{R_s}{L_s} i_d + \omega_e i_q + \dfrac{u_d}{L_s} + \omega_e \dfrac{\psi_{rq}}{L_s} \\ \dfrac{di_q}{dt} = -\dfrac{R_s}{L_s} i_q - \omega_e i_d + \dfrac{u_q}{L_s} - \omega_e \dfrac{\psi_{rd}}{L_s} \end{cases} \tag{6}$$

Since the sampling period T is small enough, the state equation (6) can be discretized by using the first-order Euler Equation. When PM demagnetization fault occurs, the current prediction model of the discretized D-PMSG can be obtained:

$$\begin{cases} i_d\,(k+1) = i_d\,(k) + \left(-R_s i_d + u_d + \omega_e \psi_{rq}\right) \dfrac{T_s}{L_s} + \omega_e i_q T_s \\ \\ i_q\,(k+1) = i_q\,(k) + \left(-R_s i_q + u_q + \omega_e \psi_{rd}\right) \dfrac{T_s}{L_s} + \omega_e i_d T_s \end{cases} \tag{7}$$

Rewrite it into the matrix form:

$$i\,(k+1) = E\,(k)\, i\,(k) + F u\,(k) + \bar{P}\,(k) \tag{8}$$

where $E(k) = \begin{bmatrix} 1 - \frac{R_s}{L_s} T_s & T_s \omega_e(k) \\ -T_s \omega_e(k) & 1 - \frac{R_s}{L_s} T_s \end{bmatrix}$, $F = \begin{bmatrix} \frac{T_s}{L_s} & 0 \\ 0 & \frac{T_s}{L_s} \end{bmatrix}$, $\bar{P}(k) = \begin{pmatrix} \frac{\psi_{rq}}{L_s} T_s \omega_e(k) \\ -\frac{\psi_{rd}}{L_s} T_s \omega_e(k) \end{pmatrix}$, $\bar{P}(k) = \begin{pmatrix} \frac{\psi_{rq}}{L_d} T_s \omega_e(k) \\ -\frac{\psi_{rd}}{L_q} T_s \omega(k) \end{pmatrix}$.

3. FAULT-TOLERANT CONTROL STRATEGY OF D-PMSG

From the preceding analysis, when PM demagnetization fault occurs, the stator current will increase. However, because the stator current cannot rise all the time, the motor speed will disjoint with the wind speed, and the motor performance will decrease. To solve this problem, a demagnetization fault-tolerant control strategy in the D-PMSG wind power generation system is proposed. It can reduce the increase of stator current so that the D-PMSG wind power generation system could operate statically even after PM demagnetization fault.

3.1. Single-Vector Model Predictive Current Control

Single-vector model predictive current control (MPCC) takes the current as the control quantity and selects a voltage vector by calculating the cost function. The voltage vector minimizes the distance between the predicted current value and the given current value. The voltage vector is the optimal voltage vector. The schematic diagram of single-vector MPCC vector selection is shown in Figure 2. Equation (3) gives the calculation equation of the predicted current value, and the selected cost function is:

$$g_i = \left|i_d^* - i_d\left(k+1\right)\right| + \left|i_q^* - i_q\left(k+1\right)\right| \tag{9}$$

where i_d^* and i_q^* are the d-axis and q-axis stator current set values; $i_d(k+1)$ and $i_q(k+1)$ are the d-axis and q-axis predicted current values.

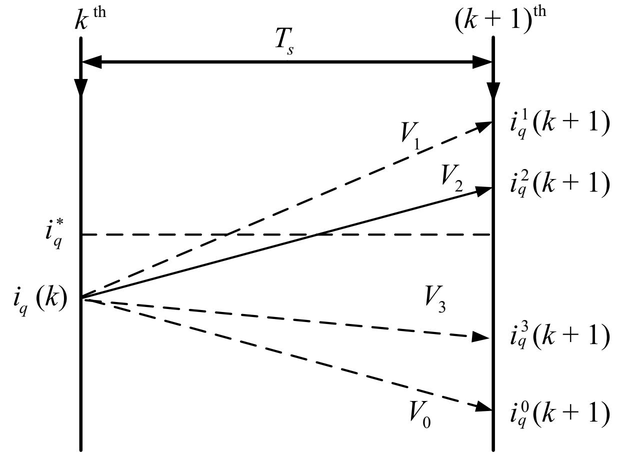

Figure 2. Schematic diagram of single-vector MPCC vector selection.

Firstly, the d-axis and q-axis component of the stator current is predicted seven times by seven voltage vectors generated by the two-level converter. Then, the predicted current value is substituted into the cost function for calculation. The voltage vector that minimizes the calculated result is the optimal voltage vector for this sampling period. Secondly, output the optimal voltage vector to the pulse generator to complete the sampling cycle. In the example in Figure 2, V_2 is selected as the optimal voltage vector, but there is still a large error between B and the given value.

3.2. Two-Vector Model Predictive Fault-Tolerant Control

The single-vector MPCC computes and outputs only one optimal voltage vector in a control cycle. However, the two-vector model predictive fault-tolerant control is based on the single-vector MPCC. And it performs a voltage vector selection to determine the second optimal voltage vector V_{opt_2}. The same cost function (9) is still used when V_{opt_2} is selected. Let the first optimal voltage vector V_{opt_1} and V_{opt_2} work together on one sampling cycle to minimize the error between the predicted value and the given value, and a better control effect can be achieved. Figure 3 shows the schematic diagram of the two-vector model predictive fault-tolerant control.

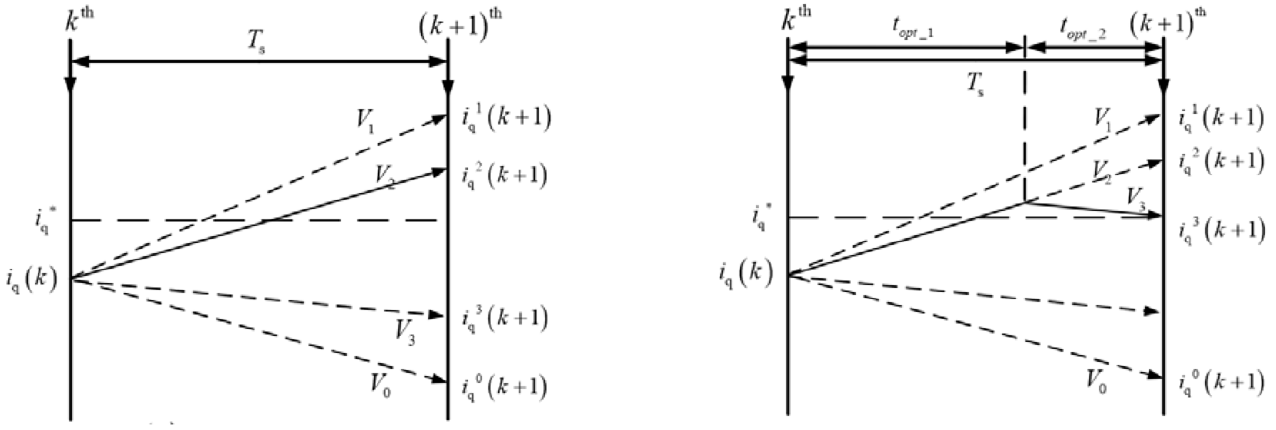

(a) (b)

Figure 3. Schematic diagram of the two-vector model predictive fault-tolerant control. (a) The first optimal vector selection. (b) The second optimal vector selection.

Following the example in Figure 3, two tasks need to be carried out simultaneously during the selection of V_{opt_2}. The first task is to assign the acting time of two voltage vectors in a sampling period, that is, to calculate V_{opt_1} and V_{opt_1} in Figure 3(b). The second task is to use the discrete model of the discretized D-PMSG under PM demagnetization fault to predict the current and calculate the two optimal voltage vectors, that is, V_2 and V_3 in Figure 3(b) are selected.

1) Assign the acting time of two voltage vectors

As the acting time of the voltage vector changes, $u(k)$ in the current prediction equation (8) under the demagnetization fault needs to be changed to:

$$u'(k) = \begin{bmatrix} t_{opt\_1} \cdot u_{d\_opt\_1} + (T_s - t_{opt\_1})\, u_{d\_j} \\ t_{opt\_1} \cdot u_{q\_opt\_1} + (T_s - t_{opt\_1})\, u_{q\_j} \end{bmatrix} \tag{10}$$

where t_{opt_1} is the acting time of the first optimal voltage vectors V_{opt_1}; $u_{d\_opt\_1}$ and $u_{q\_opt\_1}$ are the d-axis and q-axis the first optimal voltage vectors V_{opt_1}; u_{d_j} and u_{q_j} are the d-axis and q-axis the j voltage vectors V_j, $j = 1, 2, ...7$.

By substituting Equation (10) into Equation (8), a new current prediction equation under PM demagnetization fault is obtained:

$$i(k+1) = E(k)\, i(k) + Fu'(k) + \bar{P}(k) \tag{11}$$

Two-vector model predictive fault-tolerant control adopts deadbeat q-axis current control. As shown in Figure 2(b), the q-axis current at the $(k+1)^{\text{th}}$ instant should reach its set value. The deadbeat q-axis current control equation is:

$$i_q(k+1) = i_q(k) + s_{opt\_1} \cdot t_{opt\_1} + s_j (T_s - t_{opt\_1}) = i_q^* \tag{12}$$

where S_{opt_1} and S_j are the slopes of i_q when two voltage vectors V_{opt_1} and V_j operate respectively; S_{opt_1} and S_j are expressed as:

$$s_{opt\_1} = \frac{di_q}{dt}\Big|_{u_q = u_{opt\_1}} = -\frac{R_s}{L_s} i_q - \omega_e \frac{L_d}{L_s} i_d - \omega_e \frac{\psi_{rd}}{L_s} + \frac{u_{opt\_1}}{L_s} \tag{13}$$

$$s_j = \frac{di_q}{dt}\Big|_{u_q = u_{q\_j}} = -\frac{R_s}{L_s} i_q - \omega_e \frac{L_d}{L_s} i_d - \omega_e \frac{\psi_{rd}}{L_s} + \frac{u_{q\_j}}{L_s} \tag{14}$$

According to Equation (12), the equation for calculating the action time of V_{opt_1} is:

$$t_{opt\_1} = \frac{i_q^* - i_q(k) - s_j T_s}{s_{opt\_1} - s_j} \tag{15}$$

Substituting Equation (13) and Equation (14) into Equation (15), we can get:

$$t_{opt\_1} = \frac{i_q^* - i_q(k) - s_j T_s}{u_{opt\_1} - u_{q\_j}} \cdot L_s \tag{16}$$

Because the two optimal voltage vectors operate in the same period, the acting time of the second optimal voltage vector is:

$$t_{opt\_2} = T_s - t_{opt\_1} = T_s - \frac{i_q^* - i_q(k) - s_j T_s}{u_{opt\_1} - u_{q\_j}} \cdot L_s \tag{17}$$

2) Select two optimal voltage vectors

Firstly, the 7 voltage vectors generated by the two-level converter are substituted into Equation (8) to calculate the predicted current value. Substitute the result into the cost function Equation (9) for calculation, and the voltage vector that minimizes g_i after the calculation is the first optimal voltage vector V_{opt_1} of this sampling period. The first optimal voltage vector V_{opt_1} is combined with seven voltage vectors respectively, and the action times of the two voltage vectors V_{opt_1} and V_j in each combination are allocated through the first task. Then, 7 groups of predicted current values are calculated by Equation (11). The 7 groups of predicted current values are substituted into the cost function Equation (9) to obtain $7g_i$. The voltage vector combination corresponding to the predicted current value that minimizes g_i is the optimal voltage vector combination in the sampling period. The second voltage vector in the combination is the second optimal voltage vector V_{opt_2}. Two optimal voltage vectors and their action times V_{opt_1}, V_{opt_2}, t_{opt_1}, and t_{opt_2} are output to the pulse generator to complete the control of a sampling period.

3.3. EKF Flux Linkage Observer

The electromagnetic torque of the D-PMSG wind power generation system will be unbalanced instantly when a PM demagnetization fault occurs. In this case, real-time flux information needs to be obtained and fed back to the control terminal for fault-tolerant control. To conduct real-time flux observation, an EKF flux linkage observer is designed. Figure 4 is the flowchart of the EFK observer.

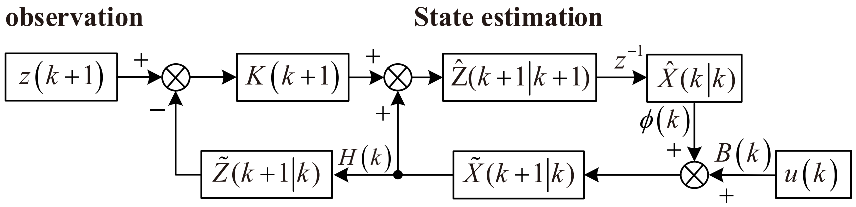

Figure 4. The flow chart of the EFK observer.

EKF observer is an extension of the Kalman filter in a nonlinear system. The state and measurement equation of the discrete nonlinear system is expressed as follows:

$$\begin{cases} x(k+1) = f[x(k), u(k)] + w(k) \\ z(k) = b[x(k)] + v(k) \end{cases} \tag{18}$$

Expand $f[x(k), u(k)]$ and $h[x(k)]$ according to the first-order Taylor series, and by replacing $f(*)$ with the Jacobian matrix, a local linear model can be obtained:

$$\begin{cases} x(k+1) = \phi(k)\, x(k) + B(k)\, u(k) + w(k) \\ z(k) = H(k)\, x(k) + v(k) \end{cases} \tag{19}$$

where $H(k) = \frac{\partial b[x(k)]*T_s}{\partial x}\big|_{x(k)=\hat{x}(k)}$; $\phi(k) = \frac{\partial\{x(k)+f[x(k),u(k)]*T_s\}}{\partial x}\big|_{x(k)=\hat{x}(k)}$; $x(k)$ is the state vector of the system; $\phi(k)$ is the state transition matrix; $B(k)$ is the control input matrix; $u(k)$ is the input vector of the system; $z(k)$ is the observation vector of the system; $H(k)$ is the state observation matrix; $w(k)$ is the process noise; $v(k)$ is the observation noise; $w(k)$ and $v(k)$ are Gaussian white noise with zero means; k is the current number of iterations.

Since the object of observation is d-axis and q-axis flux linkages, the flux linkage needs to be also a state variable. According to Equation (8), the fourth-order nonlinear surface D-PMSG coupling model is established as follows:

$$\begin{bmatrix} i_d(k+1) \\ i_q(k+1) \\ \psi_{rd}(k+1) \\ \psi_{rq}(k+1) \end{bmatrix} = \begin{bmatrix} 1-\dfrac{R_s}{L_s}T_s & T_s\omega_e(k) & 0 & 0 \\ -T_s\omega_e(k) & 1-\dfrac{R_s}{L_s}T_s & 0 & 0 \\ 0 & 0 & 1 & 0 \\ 0 & 0 & 0 & 1 \end{bmatrix} \begin{bmatrix} i_d(k) \\ i_q(k) \\ \psi_{rd}(k) \\ \psi_{rq}(k) \end{bmatrix} + \begin{bmatrix} \dfrac{T_s}{L_s} & 0 \\ 0 & \dfrac{T_s}{L_s} \\ 0 & 0 \\ 0 & 0 \end{bmatrix} \begin{bmatrix} u_d(k)+\psi_{rq}\omega_e(k) \\ u_q(k)-\psi_{rd}\omega_e(k) \end{bmatrix} \tag{20}$$

Based on the coupling model of Equation (20), to identify the d-axis and q-axis flux linkages, Equation (6) is rewritten as:

$$\frac{d}{dt}\begin{bmatrix} i_d \\ i_q \\ \psi_{rd} \\ \psi_{rq} \end{bmatrix} = \begin{bmatrix} -\dfrac{R_s}{L_s} & \omega_e & 0 & 0 \\ -\omega_e & -\dfrac{R_s}{L_s} & 0 & 0 \\ 0 & 0 & 0 & 0 \\ 0 & 0 & 0 & 0 \end{bmatrix} \begin{bmatrix} i_d \\ i_q \\ \psi_{rd} \\ \psi_{rq} \end{bmatrix} + \begin{bmatrix} \dfrac{1}{L_s} & 0 \\ 0 & \dfrac{1}{L_s} \\ 0 & 0 \\ 0 & 0 \end{bmatrix} \begin{bmatrix} u_d \\ u_q \end{bmatrix} + \begin{bmatrix} \omega_e\dfrac{\psi_{rq}}{L_s} \\ -\omega_e\dfrac{\psi_{rd}}{L_s} \\ 0 \\ 0 \end{bmatrix} \tag{21}$$

The state variable matrix of the system is $x_1 = \begin{bmatrix} i_{d1} & i_{q1} & \psi_{d1} & \psi_{q1} \end{bmatrix}^T$; the output variable matrix of the system is $z(x_1) = \begin{bmatrix} i_{d1} & i_{q1} \end{bmatrix}^T$; the system input vector is $u_1 = \begin{bmatrix} u_d & u_q \end{bmatrix}^T$.

It can be concluded that:

$$f(x_1) = \begin{bmatrix} \dfrac{-R_s i_{d1} + w_e\psi_{rq}}{L_s} + w_e i_{q1} \\ \dfrac{-R_s i_{q1} - w_e\psi_{rd}}{L_s} - w_e i_{d1} \\ 0 \\ 0 \end{bmatrix} \tag{22}$$

The Jacobian matrix can be obtained:

$$\phi = I + \frac{\partial f(x_1)}{\partial x_1} = \begin{bmatrix} 1-\dfrac{R_sT_s}{L_s} & w_eT_s & 0 & (-R_s i_{d1} + w_e\psi_{rq})T_s \\ -w_eT_s & 1-\dfrac{R_sT_s}{L_s} & -\dfrac{w_eT_s}{L_s} & -(R_s i_{q1} + w_e\psi_{rd})T_s \\ 0 & 0 & 1 & 0 \\ 0 & 0 & 0 & 1 \end{bmatrix} \tag{23}$$

where I is the identity matrix.

The measurement equation is:

$$z_1 = \begin{bmatrix} 1 & 0 & 0 & 0 \\ 0 & 1 & 0 & 0 \end{bmatrix} \begin{bmatrix} i_d \\ i_q \\ \psi_{rd} \\ \psi_{rq} \end{bmatrix} \tag{24}$$

The control input matrix is $B_1 = \begin{bmatrix} 0 & 1/L_s & 0 & 0 \\ 1/L_s & 0 & 0 & 0 \end{bmatrix}^T$, and the state observation matrix is $H_1 = \begin{bmatrix} 1 & 0 & 0 & 0 \\ 0 & 1 & 0 & 0 \end{bmatrix}$.

3.4. Improved Luenberger Mechanical Torque Observer

When the wind speed changes, the force on the blade of the wind turbine will change, and the motion equation of D-PMSG will be unbalanced instantly, resulting in speed fluctuation. This series of changes will affect the system control accuracy, response time, and other indicators. In this paper, an improved Luenberger observer is designed to observe the mechanical torque caused by the change of wind speed after the demagnetization fault. Compensation control is carried out in the speed loop according to the observation results. The construction process of the improved Luenberger mechanical torque observer is as follows.

According to Equation (2), the improved Luenberger observer equation is constructed by taking the cross-axis current as the input variable, the mechanical angular velocity as the output variable, and the observed rotational speed and observed mechanical torque as the state variables:

$$\begin{cases} \dot{\hat{x}} = A\hat{x} + Bu + H(y - \hat{y}) \\ \hat{y} = C\hat{x} \end{cases} \tag{25}$$

where $A = \begin{bmatrix} -\frac{B}{J} & \frac{1}{J} \\ 0 & 0 \end{bmatrix}$; $B = \begin{bmatrix} -\frac{1}{J} \\ 0 \end{bmatrix}$; $C = \begin{bmatrix} 1 & 0 \end{bmatrix}$; $H = \begin{bmatrix} h_1 \\ h_2 \end{bmatrix}$; $\hat{x} = \begin{bmatrix} \hat{\omega}_r \\ \hat{T}_m \end{bmatrix}$; $u = T_e$. As the feedback matrix of the system, H can improve the dynamic response of the system and make the state estimation closer to the actual value faster by observing the pole position configuration.

The error state equation of the observer is:

$$\dot{e} = (A - HC)e \tag{26}$$

where e is the state estimation error, $e = x - \hat{x}$.

The dynamic response of the observer depends on the eigenvalue of (A-HC) in Equation (27). By selecting the position of the target pole, the eigenequation of the observer can be solved, and the feedback matrix H can be determined.

Assuming that p_1 and p_2 are the target pole positions of the observer respectively, the feedback matrix H is obtained by inversely deducing the eigenvalues of the error state equation:

$$\begin{cases} h_1 = -p_1 - p_2 - B/J \\ h_2 = -p_1 p_2 / J \end{cases} \tag{27}$$

The convergence condition of the state observer error equation is that all the expected poles of the observer have negative real parts, that is, all poles should be located in the left half-plane of S, and the observer is stable at this time. The farther the pole is from the imaginary axis, the larger the feedback matrix value of the observer is, the faster the dynamic response of the observer variable is, the higher the vibration frequency, and the more sensitive the system is to signal noise, and vice versa.

In the control system, the state observer realizes digital control through discrete recursion. Assuming that the speed loop sampling period of the system is T, and combining the flux value observed by the EKF flux observer, discretizing Equation (25) can obtain the recurrence equation of the observed values of rotational speed and mechanical torque:

$$\begin{cases} \hat{\omega}_r(k+1) = (1 - Th_1)\hat{\omega}_r(k) + T\left(h_1 - \dfrac{B}{J}\right)\omega_r(k) - \dfrac{3T}{2J}P_n\left(\hat{\psi}_{rq}/\sin\gamma\right)i_q(k) + \dfrac{T}{J}\hat{T}_m(k) \\ \hat{T}_m(k+1) = \hat{T}_m(k) + Th_2\left[\omega_r(k) - \hat{\omega}_r(k)\right] \end{cases} \tag{28}$$

In this observer, the motor speed, q-axis flux linkage, and q-axis current are taken as input, and the mechanical torque observation is taken as output so that the motion equation of D-PMSG can maintain balance even as the wind speed changes when a demagnetization fault occurs. In this way, the influence of wind speed fluctuation on the D-PMSG wind power generation system can be reduced.

3.5. Algorithm Implementation

The realization process of the demagnetization fault-tolerant control strategy in the D-PMSG wind power generation system is as follows:

1) The d-axis and q-axis flux linkages $\hat{\psi}_{rd}$ and $\hat{\psi}_{rq}$ are observed by the EKF flux linkage observer.

2) The measured values of d-axis and q-axis flux linkages obtained in Step (1), stator current measurement value i_q and mechanical angular velocity ω_m are substituted into the improved Lunberger mechanical torque observer of the speed loop to obtain the observed mechanical torque $\hat{T}_m$.

3) Input the results of step (1) and step (2), the stator current measurement value i_q, the given speed n_{ref}, and the mechanical angular velocity ω_m into the speed loop controller to obtain the given value of the q-axis current component $i * q$.

4) Substitute the 7 voltage vectors generated by the two levels into Equation (8) for 7 times of prediction. The given values of the d-axis and q-axis current components $i * d$, $i * q$ and the predicted current are substituted into the cost function Equation (9) for calculation so that the minimum voltage vector of g_i is the first optimal voltage vector V_{opt_1}.

5) Equation (16) and Equation (17) are used to calculate the respective acting time of the two optimal voltage vectors in a sampling period. According to Equation (11) of a discrete model under demagnetization fault, the predicted current values of the d-axis and q-axis under seven voltage vector combinations are obtained. Substitute the result into the cost function Equation (9) to calculate $7g_i$.

6) Compare the $7g_i$ generated in step (5), select the combination of the voltage vectors that minimize g_i as two optimal voltage vectors V_{opt_1} and V_{opt_2}, and determine the acting time t_{opt_1} and t_{opt_2} of the two optimal voltage vectors V_{opt_1} and V_{opt_2} in the current sampling cycle, and output V_{opt_1}, V_{opt_2}, t_{opt_1} and t_{opt_2} to the control machine side converter of the pulse generator.

The system block diagram of the demagnetization fault-tolerant control strategy in the D-PMSG wind power generation system is shown in Figure 5. The speed outer loop adopts speed model predictive control to seek faster response speed.

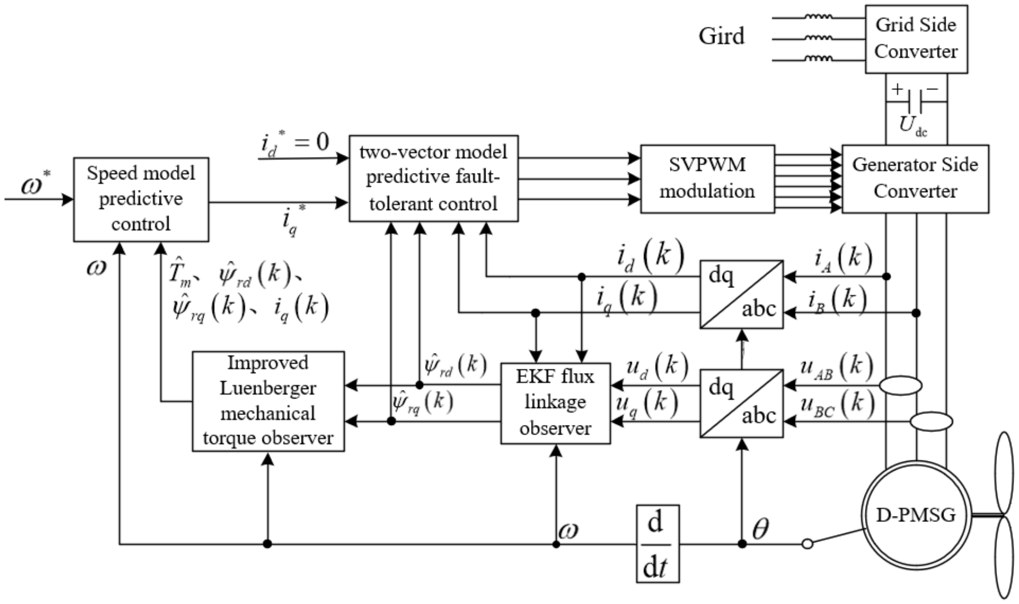

Figure 5. The system block diagram of the demagnetization fault-tolerant control strategy in D-PMSG wind power generation system.

4. EXPERIMENTAL RESULTS AND ANALYSIS

In this paper, the proposed demagnetization fault-tolerant control strategy is simulated and verified in RT-LAB semi-physical control platform based on RT-LAB built for experiments to compare with the conventional method. DSPTMS320F2812 was used as the controller, and the remaining parts of PMSG and machine side converter were simulated by RT-LAB (OP5600). The traditional D-PMSG machine side dual-closed-loop PI control and demagnetization fault-tolerant control strategy were experimentally studied. Figure 6 is the physical picture of the platform used in the experiment.

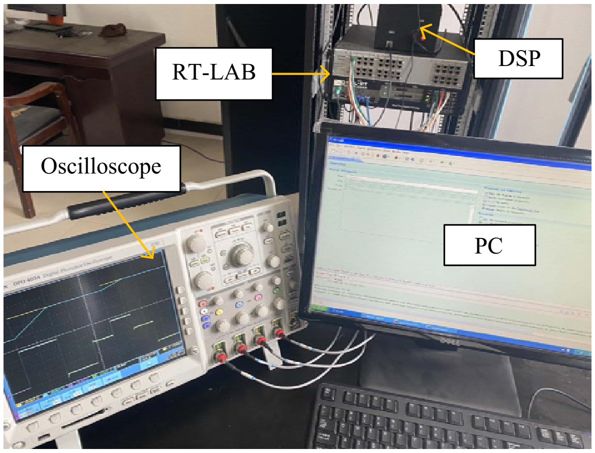

Figure 6. Rt-lab experimental platform.

Experimental motor parameters are shown in Table 1. The initial P, Q and R matrices of the EKF flux observer are selected as $P_1 = \text{diag}(1\ 1.3\ 7\ 0.9)$, $Q_1 = \text{diag}(6e-7\ 5e-7\ 1e-6\ 9e-7)$, $R_1 = \text{diag}(0.08\ 0.07)$, respectively.

The experimental conditions are set as follows: Initial given speed $\omega^* = 2000\,\text{r/min}$; Initial given mechanical torque $T_L = 6\,\text{N·m}$; Initial given PM flux linkage $\psi_{ro} = 0.12\,\text{Wb}$. To simulate the fluctuation of wind speed, the given mechanical torque T_L is increased to 12 N·m at 0.1 s; the PM loses its amplitude and angle at 0.15 s; $\psi_{ro} = 0.12\,\text{Wb}$ becomes $\psi_r = 0.08\,\text{Wb}$; and the deflection Angle γ is simultaneously changed to $\pi/6\,\text{rad}$. At 0.2 s $\sim$ 0.28 s, the given speed fluctuation was simulated with the wind speed change (0.2 s $\sim$ 0.22 s the given speed slowly increased to 2100 r/min, 0.22 s $\sim$ 0.24 s the given speed slowly decreased to 2000 r/min, 0.24 s $\sim$ 0.26 s the given speed sharply increased to 2200 r/min, the given speed reduced to 2000 r/min from 0.26 s to 0.28 s), and the given mechanical torque T_L was reduced to 8 N·at 0.32 s.

Table 1. D-PMSG parameters.

Parameters	Value
Rated power (W)	4.5 kW
Stator inductance (mH)	8.5
Stator resistance (Ω)	0.48
Rated line voltage (V)	300
Rated speed (r/min)	2000
Rotor inertia (kg·m^2)	0.003
Rated line current (A)	18
Stator current limit value (A)	42
Number of pole pairs	4

4.1. Experimental Results of Dual-Closed-Loop PI Control

The experimental results of the dual-closed-loop PI control at the engine side of the traditional D-PMSG wind power generation system are shown in Figure 12. At startup, the rotational speed waveform has an overshoot about 4%. When the given mechanical torque increases (0.1 s), the q-axis current increases to 17 A, but does not reach the limit. When the PM demagnetization fault occurs (0.15 s), the q-axis current will increase sharply to the limit 42 A, but at this time the motor is still not enough to maintain

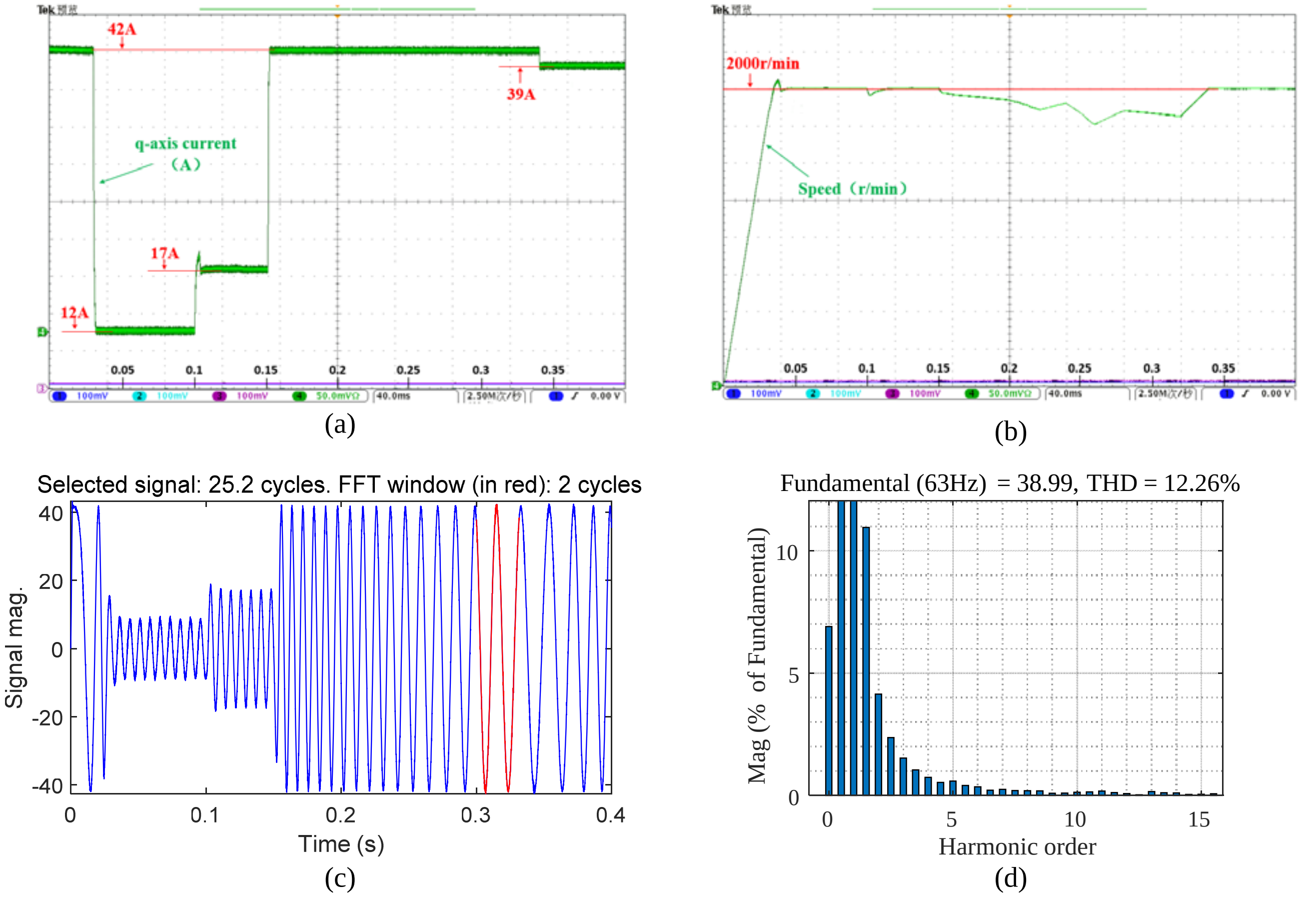

Figure 7. Experimental results of dual-closed-loop PI control. (a) The q-axis current. (b) Speed. (c) A phase current. (d) Fourier analysis.

the stability of electromagnetic torque, so the electromagnetic torque will decrease to a certain extent, and the motor speed will also decrease. When the given speed changes ($0.22\,\mathrm{s} \sim 0.28\,\mathrm{s}$), the motor speed cannot follow the given speed, and the motor speed decreases faster when the given speed increases. When the given mechanical torque decreases ($0.32\,\mathrm{s}$), the motor can be raised to the given speed of $2000\,\mathrm{r/min}$. Figure 12(d) is the Fourier analysis of the A-phase current at $0.3\,\mathrm{s}$, and the total harmonic distortion (THD) is 12.26%. As can be seen from Figure 7, the experimental results are consistent with the conclusions of the previous analysis.

4.2. Experimental Results of the Demagnetization Fault-Tolerant Control Strategy

In the case of the demagnetization fault of D-PMSG, the experimental waveform of the demagnetization fault-tolerant control strategy in D-PMSG wind power generation system is shown in Figures 8–11. The experimental results of flux linkage observation by the EKF flux linkage observer designed in this paper are shown in Figure 8. When the motor has a loss of magnetic fault ($0.15\,\mathrm{s}$), the d-axis flux linkage decreases from $0.12\,\mathrm{WB}$ to $0.06\,\mathrm{WB}$. However, the q-axis flux linkage increases from $0\,\mathrm{Wb}$ to $0.04\,\mathrm{WB}$ because of deflection angle γ, and gradually approaches the stable value in a relatively short time, achieving a better observation effect.

The experimental waveform of q-axis current and speed of the demagnetization fault-tolerant control strategy is shown in Figure 9. Compared with the dual-closed-loop PI control, when the PM demagnetization faults ($0.15\,\mathrm{s}$), the increased range of the q-axis current decreases, and the increased range does not exceed the limit of the stator current. When the given speed increases ($0.2\,\mathrm{s}$, $0.24\,\mathrm{s}$), the q-axis current increases within the limit of the stator current. As can be seen from Figure 7(b)

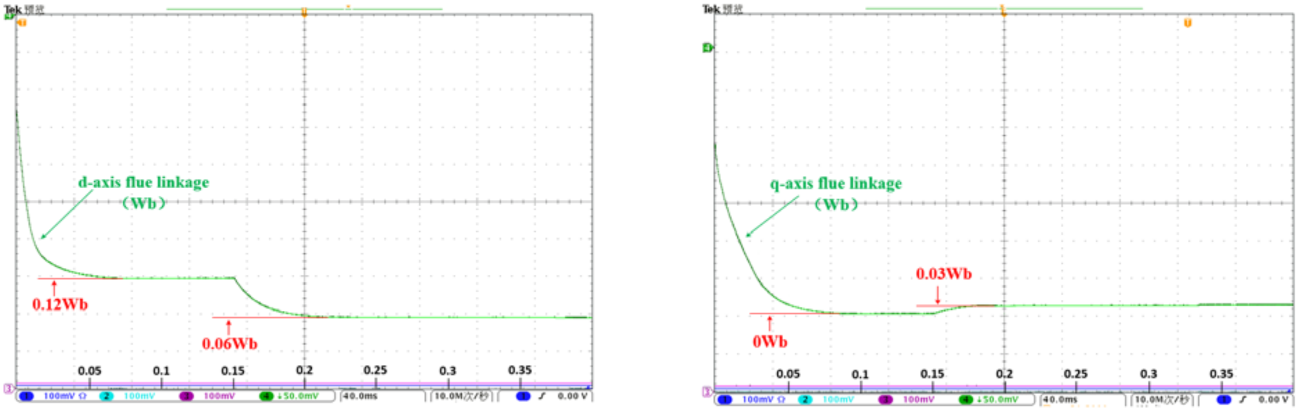

(a) (b)

Figure 8. EKF flux observer observation results. (a) The d-axis flue linkage. (b) The q-axis flue linkage.

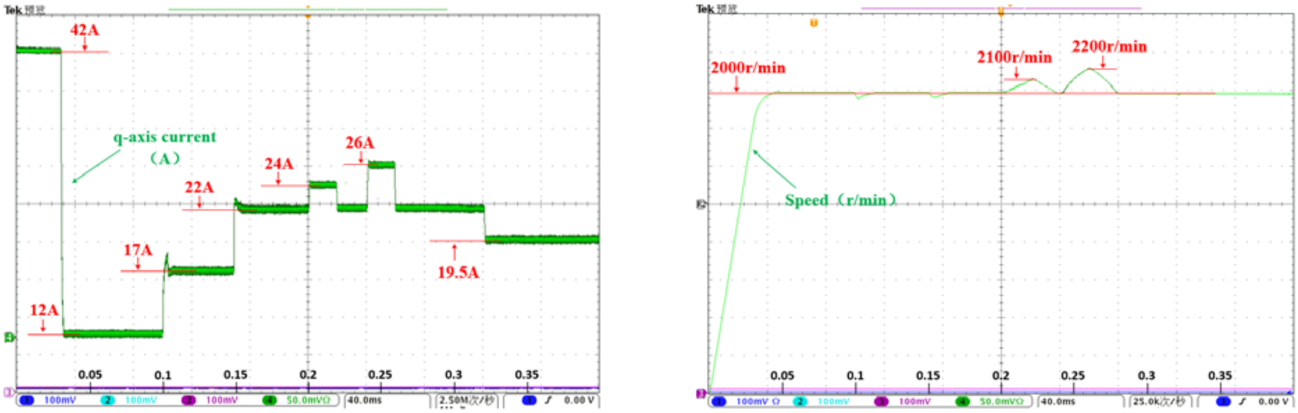

(a) (b)

Figure 9. Experimental waveform of the speed of the demagnetization fault-tolerant control strategy. (a) The q-axis current. (b) Speed.

and Figure 9(b), when the given mechanical torque increases for 0.1 s, the rotation speed fluctuation of dual-closed-loop PI control is 50 r/min, and the time from the beginning of the drop to the recovery to the steady state is 16 ms. The speed fluctuation of the demagnetization fault-tolerant control strategy is 40 r/min, and the time from the initial drop to the recovery to the steady state is 12 ms. When the given mechanical torque decreases (0.32 s), the motor speed of the demagnetization fault-tolerant control strategy has a small jitter (10 r/min), but the motor speed is only restored to the steady-state value at 2 ms. The data comparison shows that when the given mechanical torque changes (0.1 s and 0.32 s), the speed waveform overshoot is smaller, and the fluctuation time is shorter by adopting the demagnetization fault-tolerant control strategy. It reflects that the demagnetization fault-tolerant control strategy has good dynamic response characteristics and anti-interference ability. After using the demagnetization fault-tolerant control strategy, when a given speed changes (0.2 s ∼ 0.28 s), the motor can also match the given speed, which reflects the good following of wind speed changes.

The A-phase current and harmonic analysis diagram of the magnetization fault-tolerant control strategy is shown in Figure 10. Compared with the dual-closed-loop PI control, the increased amplitude of the A-phase current decreases when the motor has A magnetization loss fault (0.15 s). Figure 10(a) is the A-phase current. The red part of Figure 10(a) indicates that the harmonic analysis was performed from 0.3 s. Figure 10(b) is the Fourier analysis diagram of the A-phase current at 0.3 s. The total

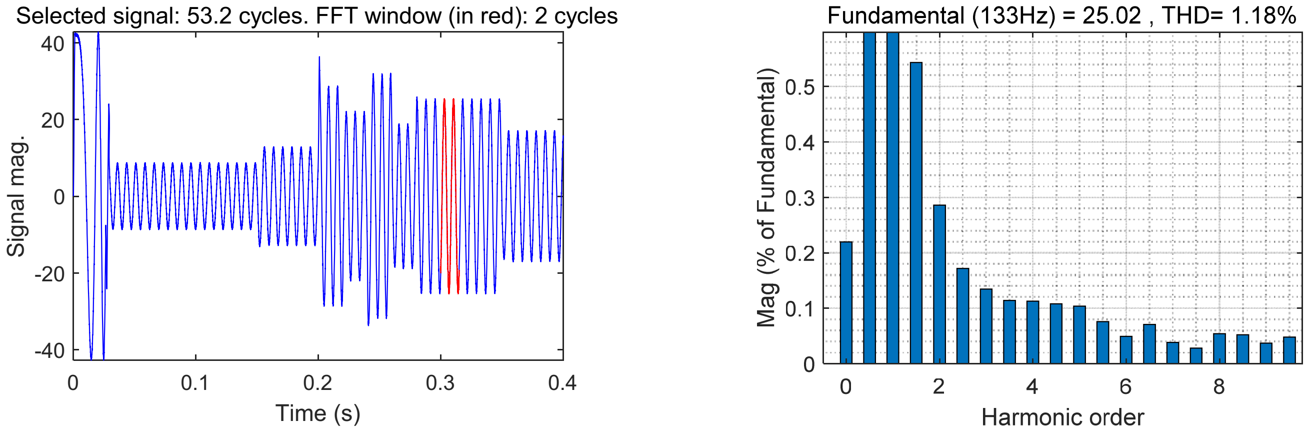

(a) (b)

Figure 10. The A-phase current and harmonic analysis diagram of the magnetization fault-tolerant control strategy. (a) A phase current. (b) Fourier analysis.

harmonic distortion (THD) is 1.18%, which is significantly reduced compared to the THD controlled by dual-closed-loop PI control.

The observed mechanical torque simulation results of the magnetization fault-tolerant control strategy are shown in Figure 11. Because the improved Luenberger torque observer uses parameters such as observed flux linkage and motor speed in the calculation, the observed mechanical torque has a slight jitter when the motor loses magnetism (0.15 s), and the given speed increases (0.2 s and 0.24 s). However, after a short period (8 ∼ 20 ms), the observed mechanical torque remains at a stable value (12 N·m). When the mechanical torque decreases (0.32 s), the observer still has good observability. The simulation results show that the designed observer can still observe the mechanical torque after the occurrence of the demagnetization fault and that the proposed control strategy has better fault tolerance performance.

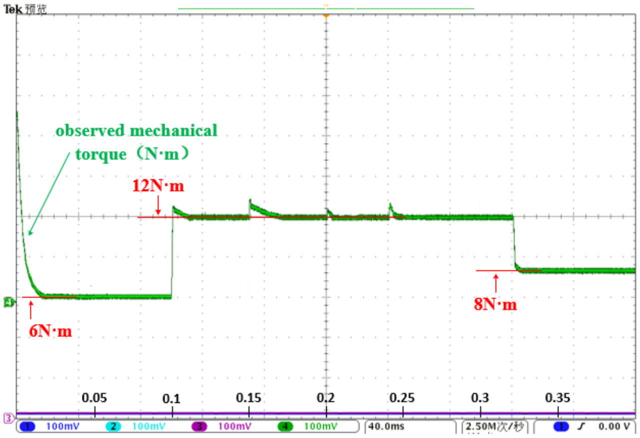

Figure 11. The observed mechanical torque simulation results of the magnetization fault-tolerant control strategy.

As can be seen from the experimental results, compared with the dual-closed-loop PI control, the proposed control strategy has stronger fault tolerance, less rotational speed fluctuation, and better dynamic response when the mechanical torque changes, which is more in line with the actual operation of D-PMSG.

5. CONCLUSION

Aiming at the problem of motor speed decrease in D-PMSG wind power generation system after PM demagnetization faults, a demagnetization fault-tolerant control strategy in D-PMSG wind power generation system was proposed. After the comparison of the experiment with traditional D-PMSG wind power generation system dual-closed-loop PI control, the following conclusions are drawn:

1) The dual-closed-loop PI control has limited fault tolerance under the PM demagnetization faults. Its q-axis current cannot increase infinitely so that the electromagnetic torque equation cannot maintain balance, and the motor speed cannot follow the given speed. The motor will run at a reduced speed. In this paper, an EKF observer is designed to observe the PM flux linkage and feed it into the two-vector model predictive fault-tolerant controller. The controller selects the voltage vector twice in each sampling period so that the cost function can get the optimal voltage vector in a larger range. These methods can reduce the amplitude of q-axis current increase, to achieve the purpose of demagnetization fault-tolerant control. The experimental results show that the two-vector model predictive fault-tolerant control strategy can keep the speed stable when the demagnetization fault occurs, achieve a better flux linkage observation effect, and have a stronger fault-tolerant ability.

2) After receiving the flux parameters provided by the EKF observer, an improved Luenberger mechanical torque observer was designed to observe the mechanical torque of D-PMSG in real-time. And the observed mechanical torque is input into the speed model predictive control to reduce the vibration caused by the change of wind speed on the motor speed. The experimental results show that the speed waveform of the control strategy using the improved Luenberger mechanical torque observer is more stable, and the anti-interference ability is stronger.

ACKNOWLEDGMENT

This work was supported by the National Natural Science Foundation of China under Grant Number 51907061, Educational Commission of Hunan Province of China under Grant Number 21B0552.

REFERENCES

1. Pang, S., X. Zheng, H. Li, Y. Liu, and Y. Feng, "Passivity full-order sliding mode control for DFIG wind turbine system," *IECON 2017 — 43rd Annual Conference of the IEEE Industrial Electronics Society*, 8236–8240, 2017, doi: 10.1109/IECON.2017.8217445.
2. Hou, L., X. Zheng, C. Wang, Y. Li, and H. Li, "Based on PCHD and HPSO sliding mode control of D-PMSG wind power system," *2018 International Power Electronics Conference (IPEC-Niigata 2018 — ECCE Asia)*, 2901–2906, 2018, doi: 10.23919/IPEC.2018.8507616.
3. Imad, A., S. El Hani, A. Echchaachouai, and A. A. Energy, "Robust active disturbance rejection control of a direct driven PMSG wind turbine," *2017 International Renewable and Sustainable Energy Conference (IRSEC)*, 1–6, 2017, doi: 10.1109/IRSEC.2017.8477283.
4. He, S. and M. Wang, "Grey prediction pi control of direct drive permanent magnet synchronous wind turbine," *2020 IEEE 4th Conference on Energy Internet and Energy System Integration (EI2)*, 2032–2035, 2020, doi: 10.1109/EI250167.2020.9346881.
5. Barmpatza, A. C. and J. C. Kappatou, "Study of a combined demagnetization and eccentricity fault in an AFPM synchronous generator," *Energies*, 2020.
6. Ismagilov, F. R., V. Vavilov, D. Gusakov, A. Kh. Miniyarov, and V. V. Ayguzina, "Diagnostic method of rotor cracks and local demagnetization by using the measuring coils for the permanent magnet synchronous machines," *Progress In Electromagnetics Research C*, Vol. 86, 123–136, 2018.
7. Mohammed, E., G. Kobet, and A. Eltom, "Investigation of a new method for synchronous generator loss of excitation protection," *2019 IEEE Power & Energy Society General Meeting (PESGM)*, 1–5, IEEE, 2019.
8. Lu, W., H. Zhao, and S. Liu, "Demagnetization conditions comparison for line-start permanent magnet synchronous motors," *2014 17th International Conference on Electrical Machines and Systems (ICEMS)*, 48–52, 2014, doi: 10.1109/ICEMS.2014.7013449.

9. Kim, D.-H., K. S. Kim, I.-J. Yang, J. Lee, and W.-H. Kim, "Alternative bridge spoke permanent magnet synchronous generator design for wind power generation systems," *IEEE Access*, Vol. 9, 152819–152828, 2021, doi: 10.1109/ACCESS.2021.3127556.
10. Mínaz, M. R. and E. Akcan, "An effective method for detection of demagnetization fault in axial flux coreless PMSG with texture-based analysis," *IEEE Access*, Vol. 9, 17438–17449, 2021, doi: 10.1109/ACCESS.2021.3050418.
11. Huan, J. and H. Zhu, "Design of the outer-rotor coreless bearingless permanent magnet synchronous generator based on an improved MOPSO algorithm," *Progress In Electromagnetics Research M*, Vol. 110, 11–24, 2022.
12. Zhu, H., K. Zhou, and J. Huan, "Compensation rotor vibration of outer rotor coreless bearingless permanent magnet synchronous generator using variable step least mean square adaptive filter," *Progress In Electromagnetics Research M*, Vol. 106, 191–203, 2021.
13. Zhou, B., G. Tang, and Y. Luo, "Dynamic modeling and analysis of demagnetizing rotor of permanent magnet synchronous motor," *Shock and Vibration*, 2021.
14. Song, X., J. Zhao, J. Song, et al., "Local demagnetization fault recognition of permanent magnet synchronous linear motor based on S-transform and PSO-LSSVM," *IEEE Transactions on Power Electronics*, Vol. 35, No. 8, 7816–7825, 2020.
15. Barmpatza, A. C. and J. C. Kappatou, "Study of the total demagnetization fault of an AFPM wind generator," *IEEE Transactions on Energy Conversion*, 2020.
16. Huang, G., J. Li, E. F. Fukushima, et al., "An improved equivalent-input-disturbance approach for PMSM drive with demagnetization fault," *ISA Transactions*, 2020.
17. Zhao, K., R. Zhou, J. T. She, et al., "Demagnetization-fault reconstruction and tolerant-control for PMSM using improved SMO-based equivalent-input-disturbance approach," *IEEE/ASME Transactions on Mechatronics*, 2021.
18. Lin, L., X. Zhang, W. Guo, et al., "Analysis on loss-of-excitation process and research on protection method of synchronous generators," *High Voltage Engineering*, Vol. 40, No. 11, 3544–3553, 2014.
19. Zhang, Z., H. Zhang, T. Yue, et al., "Diagnosis of PMSG demagnetization degree based on fuzzy neural network," *Micromotors*, Vol. 52, No. 11, 27–30, 2019, doi: 10.15934/j.cnki.micromotors.2019.11.006.
20. Imad, A., S. El Hani, A. Echchaachouai, and A. A. Energy, "Robust active disturbance rejection control of a direct driven PMSG wind turbine," *2017 International Renewable and Sustainable Energy Conference (IRSEC)*, 1–6, 2017, doi: 10.1109/IRSEC.2017.8477283.
21. Cui, S., B. Du, and S. Han, "A diagnosis for demagnetization of permanent magnetic synchronous motor based on second order generalized integrator," *2015 IEEE Vehicle Power and Propulsion Conference (VPPC)*, 1–5, 2015, doi: 10.1109/VPPC.2015.7352874.
22. Quintal-Palomo, R. E., M. Flota-Bañuelos, A. Bassam, R. Peón-Escalante, F. Peñuñuri, and M. Dybkowski, "Post-fault demagnetization of a PMSG under field oriented control operation," *IEEE Access*, Vol. 9, 53838–53848, 2021, doi: 10.1109/ACCESS.2021.3070531.
23. Usman, A., V. K. Sharma, and B. S. Rajpurohit, "Harmonic analysis of a BLDC motor under demagnetization fault conditions," *2020 IEEE 9th Power India International Conference (PIICON)*, IEEE, 2020.
24. Verkroost, L., J. De Bisschop, H. Vansompel, F. De Belie, and P. Sergeant, "Active demagnetization fault compensation for axial flux permanent-magnet synchronous machines using an analytical inverse model," *IEEE Transactions on Energy Conversion*, Vol. 35, No. 2, 591–599, Jun. 2020, doi: 10.1109/TEC.2019.2958071.